SIMULATION OF TOTAL HARMONIC DISTORTION OF A MEMS LOUDSPEAKER WITH A FEEDBACK LOOP USING A STATE SPACE MODEL

Romain Liechti[1], Fabrice Casset[1], Christel Dieppedale[1], Stéphane Durand[1]
[1] *CEA-Leti, Univ. Grenoble Alpes, F-38000 Grenoble, France*

Abstract

Since MEMS loudspeakers are significantly smaller than conventional devices, they require larger membrane displacements to achieve the same sound pressure level. In piezoelectric actuators, this often means applying higher input voltages, both of which increase non-linear distortion. In this paper, we present an active control scheme that integrates a collocated sensor and actuator within the MEMS loudspeaker. Using feedback control, the system compensates for non-linear contributions to the output waveform in real time, reducing total harmonic distortion while maintaining acoustic performance. Device and system-level modeling are used to demonstrate the feasibility of this approach for MEMS transducers intended for in-ear applications.

Keywords: *MEMS loudspeaker, piezoelectric actuator, active control, state space model, total harmonic distortion*

1. Introduction

MEMS loudspeakers are promising candidates for next-generation in-ear headphones and hearing aids due to their compact size, low power consumption, and compatibility with CMOS fabrication [1]. Their miniaturized structure allows for highly integrated devices, but it also introduces pronounced nonlinearities that manifest as harmonic distortion. A standard metric for assessing this characteristic is Total Harmonic Distortion (THD), defined as the ratio between the combined power of all higher-order harmonics and the total signal power. Prior research indicates that human auditory perception can detect THD levels as low as 0.1%, depending on the specific order of the generated harmonics [2], [3], [4].

Conventional approaches to reducing distortion rely on structural optimization, such as tailoring diaphragm shapes, suspension geometries, or electrode layouts [5], [6]. While these methods improve linearity, they are static and cannot adapt to variations in acoustic loading or mechanical and material related changes due to device aging and some of them rely on the shaping of the pressure response rather that reducing the intrinsic nonlinearities of the transducer.

Digital signal processing techniques offer compensation by applying pre-distortion or feedforward to the drive signal [7]. For example, feedforward compensation was used to reduce air-related nonlinear distortion in horns [8] or more recently to compensate for hysteresis in piezoelectric loudspeaker [9]. However, these open-loop methods require precise characterization of the loudspeaker to determine the filter parameters.

Active closed-loop control provides a different approach. Unlike pre-distortion or feedforward, closed-loop control works in a wider range of tolerances and does not require precise characterization of the device, but it requires an embedded sensor. In macro loudspeakers, a velocity sensor with a feedback controller was shown to be effective [10]. In the MEMS field, nested closed-loop control was successfully used for micromirrors [11].

The motivation for pursuing active control in MEMS in-ear loudspeakers is to achieve high-fidelity audio while providing adaptive compensation for acoustic loading and device aging. This work investigates the integration of sensing and closed-loop control in MEMS loudspeakers, highlighting design considerations and potential improvements in distortion reduction.

2. Concept

This study is based on a variation of the MEMS loudspeaker presented in [12] and described more extensively in [13]. The primary difference compared to the original design is the inclusion of a collocated sen-

Corresponding author: *romain.liechti@cea.fr.*

sor on the actuator. As depicted in Figure 1a, the loudspeaker is fabricated across two separate wafers. The top wafer features a stiffened square plate that moves freely along the z-axis and is separated from the frame by a narrow interstice, where dominant viscous effects prevent an acoustic short circuit. The bottom wafer consists of a device layer accomodating wide cantilever-like actuators. These actuators are built from a 12 µm elastic layer paired with a piezoelectric material sandwiched between top and bottom platinum electrodes. Within this piezoelectric layer, a collocated sensor with additional connection pads is located on the clamped side of the actuator, as depicted in Figure 1b. The sensor thus does not affect the displacement or the geometry of the loudspeaker, but the piezoelectric effect creates a voltage proportional to this displacement.

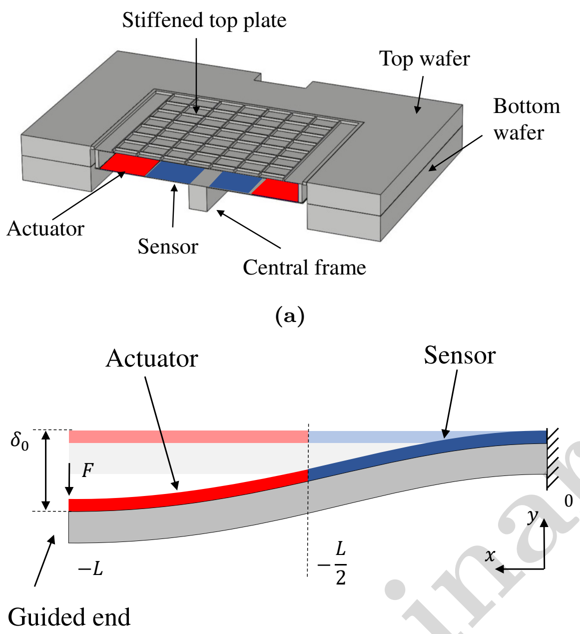

Figure 1: Cross-sectional schematics of the actuator: (a) three-dimensional view, and (b) two-dimensional cross section.

3. Modeling

As with most electroacoustics devices and more recently electroacoustics MEMS, equivalent electrical circuits provide an efficient approach to model and simulate system behavior [14]. In this study, the loudspeaker is represented using a circuit similar to those described in [12] and [15]. The equivalent electrical circuit of the loudspeaker is depicted in Figure 2, where the collocated sensor is modeled using an additional transformer of ratio γ_{s}. This multi-domain model integrates the electrical, mechanical, and acoustical behavior of the transducer connected to an IEC 60318-4 ear-occluded coupler, which represents the acoustic load of the average human ear.

The modeling begins with the beam carrying both an actuator and a sensor, as illustrated in Fig. 1b. Following a procedure comparable to that in [13], the beam is divided into two separate elements. In this case, both beams have the same moment of inertia and the same equivalent Young modulus.

Table 1: Table of lumped elements circuits parameters

Parameter	Value	Unit
R_{ga}	1	mΩ
C_{pa}	97	nF
R_{gs}	1	mΩ
C_{ps}	39	nF
R_{m}	$5 \cdot 10^{-3}$	$\mathrm{N\,s\,m^{-1}}$
M_{m}	3.6	mg
C_{m}	$3 \cdot 10^{-3}$	$\mathrm{m\,N^{-1}}$
Q_{m}	20	-
S_d	12	$\mathrm{mm^2}$
L_1	82.9	$\mathrm{Pa\,s^2\,m^{-3}}$
L_2	9400	$\mathrm{Pa\,s^2\,m^{-3}}$
L_3	130.3	$\mathrm{Pa\,s^2\,m^{-3}}$
L_4	983.8	$\mathrm{Pa\,s^2\,m^{-3}}$
L_5	133.4	$\mathrm{Pa\,s^2\,m^{-3}}$
R_1	50.6	$\mathrm{MPa\,s\,m^{-3}}$
R_2	31.1	$\mathrm{MPa\,s\,m^{-3}}$
C_1	1	$\mathrm{pPa\,m^{-3}}$
C_2	1.9	$\mathrm{pPa\,m^{-3}}$
C_3	1.5	$\mathrm{pPa\,m^{-3}}$
C_4	2.1	$\mathrm{pPa\,m^{-3}}$
C_5	1.517	$\mathrm{pPa\,m^{-3}}$

3.1. Beam model and circuit parameters

The apparent compliance C_{m} and the transduction factors γ_a and γ_s of the collocated actuator-sensor pair are obtained from a Bernoulli beam formulation of the two-beam assembly shown in Fig. 1b, with continuity of deflection, rotation, moment and shear enforced at the junction between the beams at $x = -L/2$.[1] Solving the resulting boundary-value problem for the clamped-guided and clamped-clamped cases yields the blocked force F_{bl} and the free-end displacement δ_0, from which the apparent compliance follows as

$$\frac{\delta_0}{F_{bl}} = C_{\mathrm{m}} = \frac{6\mathrm{EI}}{L^3}, \tag{1}$$

where EI is the equivalent bending stiffness of the beam assembly and L its total length. Similarly, the actuator transduction factor is given by

$$\gamma_a = \frac{6 z_{\mathrm{P}} \alpha (1-\alpha)}{L}, \tag{2}$$

with z_{P} the piezoelectric moment arm and α the length ratio between the actuator and sensor sections. Because the sensor generates no torque of its own, the

[1]The complete derivation, together with its validation against 2D finite-element simulations in COMSOL Multiphysics®, will be presented in a forthcoming publication.

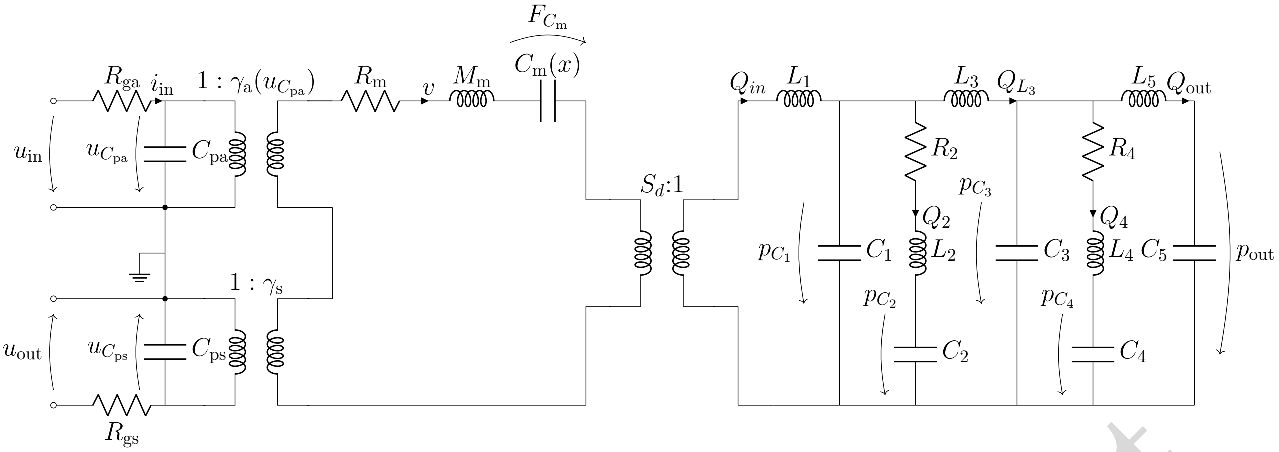

Figure 2: Multi-domains equivalent electrical circuits of the loudspeaker with a collocated sensor in an IEC 60318-4 ear-occluded coupler. R_ga and R_gs are the resistances of the electrical path for the actuator and sensor, respectively; C_pa and C_ps are the electrical capacitances of the piezoelectric layer for the actuator and sensor, respectively; γ_s and γ_a are the transduction factors for the sensor and actuator, respectively; R_m is the viscous mechanical resistance, M_m is the equivalent mass, and C_m is the apparent compliance. The transformer of ratio S_d represents the conversion from the mechanical domain to the acoustical domain. Components C_1 to C_5, L_1 to L_5 and R_2 and R_4 represent the acoustic compliances, masses and viscous damping from the ear-occluded coupler, representing themselves the acoustic impedance of the average human ear and are given in Table 1.

stress it experiences results only from the passive bending induced by the actuator, finite-element evaluation of this stress ratio gives $\gamma_\mathrm{a} = 8.3\,\gamma_\mathrm{s}$, confirming that the sensor responds linearly over the actuator's range of motion. Parameters used in this calculation are summarized in Table 2.

Table 2: Parameters used for the computation of C_m and the transduction factors γ_a and γ_s

Symbol	Value	Unit
W_a	5.8	mm
L_a	1.14	mm
W_h	10	µm
t_m	12	µm
t_p	2	µm
E_m	166	GPa
E_p	82	GPa
$e_{31,f}$	17.5	$\mathrm{C\,m^{-2}}$

The piezoelectric capacitances $C_\mathrm{pa} = C_\mathrm{ps}$ follow from the effective relative permittivity ε_r of the piezoelectric layer along the 3–1 coupling direction and the standard capacitor relation $C_p = 2W_aL_a\varepsilon_0\varepsilon_r/t_p$. The moving mass M_m is obtained from the material densities and CAD geometry, and the viscous mechanical resistance R_m is estimated from a Poiseuille flow model of the air gap surrounding the plate, following an approach similar to [15]. The resulting lumped-element parameters used in the equivalent circuit of Fig. 2 are summarized in Table 1. Non linear functions relating γ_a with u_{C_pa} and C_m with the displacement δ are taken from [16].

3.2. Open loop

The electrical equivalent circuit of Fig. 2 can be solved using a state-space equation of the form

$$\dot{\mathbf{x}} = \mathbf{A}\mathbf{x} + \mathbf{B}\mathbf{u}. \tag{3}$$

which describes the open loop system. The state vector $\mathbf{x}$ is composed of u_{C_pa}, the voltage across the actuator capacitor C_pa, u_{C_ps}, the voltage across the sensor capacitor C_ps, F_{C_m}, the force across the apparent compliance C_m, p_{C_1}, Q_2, p_{C_2}, Q_{L_3}, p_{C_3}, Q_4, p_{C_4}, the pressures and volume velocities of the ear-occluded coupler and p_out, the output pressure at the ear-occluded coupler microphone. The resulting matrix $\mathbf{A}$ is given in Equation 7. The system can be solved via a bilinear transform or a built-in state-space solver using any input signal u_in using

$$\mathbf{A}_d = \left(\mathbf{I} - \frac{1}{2}\mathbf{A}T_s\right)^{-1}\left(\mathbf{I} + \frac{1}{2}\mathbf{A}T_s\right) \tag{4}$$

and

$$\mathbf{B}_d = \left(\mathbf{I} - \frac{1}{2}\mathbf{A}T_s\right)^{-1}\mathbf{B}T_s \tag{5}$$

with $T_s = 1/f_s$ the sampling period. Samples $\mathbf{x}$(k+1) are then computed for each step using

$$\mathbf{x}(k+1) = \mathbf{A}_d\mathbf{x}(k) + \mathbf{B}_d\mathbf{u}(k). \tag{6}$$

3.3. Closed-Loop

The closed-loop architecture is depicted in Figure 3. The control scheme combines a feedforward gain K_ff acting on the command signal r with a proportional

$$
\mathbf{A} = \begin{bmatrix}
-\frac{1}{R_{\mathrm{ga}}C_{\mathrm{pa}}(u_{C_{\mathrm{pa}}})} & 0 & -\frac{\gamma_{\mathrm{a}}(u_{C_{\mathrm{pa}}})}{C_{\mathrm{pa}}(u_{C_{\mathrm{pa}}})} & 0 & 0 & 0 & 0 & 0 & 0 & 0 & 0 & 0 & 0 & 0 \\
0 & 0 & -\frac{\gamma_{\mathrm{s}}(u_{C_{\mathrm{ps}}})}{C_{\mathrm{ps}}(u_{C_{\mathrm{ps}}})} & 0 & 0 & 0 & 0 & 0 & 0 & 0 & 0 & 0 & 0 & 0 \\
\frac{\gamma_{\mathrm{a}}(u_{C_{\mathrm{pa}}})}{M_{\mathrm{m}}+S_d^2L_1} & -\frac{\gamma_{\mathrm{s}}(u_{C_{\mathrm{ps}}})}{M_{\mathrm{m}}+S_d^2L_1} & -\frac{R_{\mathrm{m}}}{M_{\mathrm{m}}+S_d^2L_1} & 0 & -\frac{1}{M_{\mathrm{m}}+S_d^2L_1} & -\frac{S_d}{M_{\mathrm{m}}+S_d^2L_1} & 0 & 0 & 0 & 0 & 0 & 0 & 0 & 0 \\
0 & 0 & 1 & 0 & 0 & 0 & 0 & 0 & 0 & 0 & 0 & 0 & 0 & 0 \\
0 & 0 & \frac{1}{C_{\mathrm{m}}(\delta)} & 0 & 0 & 0 & 0 & 0 & 0 & 0 & 0 & 0 & 0 & 0 \\
0 & 0 & \frac{S_d}{C_1} & 0 & 0 & 0 & -\frac{1}{C_1} & 0 & -\frac{1}{C_1} & 0 & 0 & 0 & 0 & 0 \\
0 & 0 & 0 & 0 & 0 & \frac{1}{L_2} & -\frac{R_2}{L_2} & -\frac{1}{L_2} & 0 & 0 & 0 & 0 & 0 & 0 \\
0 & 0 & 0 & 0 & 0 & 0 & \frac{1}{C_2} & 0 & 0 & 0 & 0 & 0 & 0 & 0 \\
0 & 0 & 0 & 0 & 0 & \frac{1}{L_3} & 0 & 0 & 0 & -\frac{1}{L_3} & 0 & 0 & 0 & 0 \\
0 & 0 & 0 & 0 & 0 & 0 & 0 & 0 & \frac{1}{C_3} & 0 & -\frac{1}{C_3} & 0 & -\frac{1}{C_3} & 0 \\
0 & 0 & 0 & 0 & 0 & 0 & 0 & 0 & 0 & \frac{1}{L_4} & -\frac{R_4}{L_4} & -\frac{1}{L_4} & 0 & 0 \\
0 & 0 & 0 & 0 & 0 & 0 & 0 & 0 & 0 & 0 & \frac{1}{C_4} & 0 & 0 & 0 \\
0 & 0 & 0 & 0 & 0 & 0 & 0 & 0 & 0 & \frac{1}{L_5} & 0 & 0 & 0 & -\frac{1}{L_5} \\
0 & 0 & 0 & 0 & 0 & 0 & 0 & 0 & 0 & 0 & 0 & 0 & \frac{1}{C_5} & 0
\end{bmatrix} \tag{7}
$$

feedback gain K_p operating directly on the filtered sensor voltage x_{16}.

Starting from the 14-state open-loop model dynamics $\dot{\mathbf{x}}_{1:14} = \mathbf{A}\mathbf{x}_{1:14} + \mathbf{B}u_{C_{\mathrm{pa}}}$, the open-loop input vector is defined as $\mathbf{B} = \left[\frac{1}{C_{\mathrm{pa}}R_{\mathrm{ga}}}, 0, \ldots, 0\right]^T$.

The measured physical signal passed to the filter is the sensor voltage $x_2 = u_{C_{\mathrm{ps}}}$. To condition this signal, it is passed through a second-order bandpass filter comprising a high-pass stage with cutoff frequency ω_l and a low-pass stage with cutoff frequency ω_h:

$$
H_{\mathrm{hp}}(s) = \frac{s}{s+\omega_l}, \quad H_{\mathrm{lp}}(s) = \frac{\omega_h}{s+\omega_h}. \tag{8}
$$

Introducing state x_{15} for the high-pass stage and state x_{16} for the low-pass stage yields the filter state equations:

$$
\dot{x}_{15} = \dot{x}_2 - \omega_l x_{15} = (\mathbf{A}_{\mathrm{row2}}\mathbf{x}_{1:14} + B_2 u) - \omega_l x_{15}, \tag{9}
$$

$$
\dot{x}_{16} = \omega_h(x_{15} - x_{16}). \tag{10}
$$

Using the filtered state x_{16}, the control law driving the actuator is defined as:

$$
u_{C_{\mathrm{pa}}} = K_{\mathrm{ff}}r - K_p x_{16}. \tag{11}
$$

Appending the two filter states to the open-loop model forms the 16-state augmented vector $\mathbf{x}_{\mathrm{aug}} = [\mathbf{x}_{1:14}^T, x_{15}, x_{16}]^T$. Substituting (11) into the open-loop and filter dynamics leads to the full closed-loop system:

$$
\dot{\mathbf{x}}_{\mathrm{aug}} = \mathbf{A}_{\mathrm{aug}}\mathbf{x}_{\mathrm{aug}} + \mathbf{B}_{\mathrm{aug}}r, \tag{12}
$$

which expands explicitly into matrix form as

$$
\begin{aligned}
\begin{bmatrix} \dot{\mathbf{x}}_{1:14} \\ \dot{x}_{15} \\ \dot{x}_{16} \end{bmatrix} &= \begin{bmatrix} \mathbf{A} & \mathbf{0} & -\mathbf{B}K_p \\ \mathbf{A}_{\mathrm{row2}} & -\omega_l & -B_2K_p \\ \mathbf{0} & \omega_h & -\omega_h \end{bmatrix} \begin{bmatrix} \mathbf{x}_{1:14} \\ x_{15} \\ x_{16} \end{bmatrix} \\
&\quad + \begin{bmatrix} \mathbf{B}K_{\mathrm{ff}} \\ B_2K_{\mathrm{ff}} \\ 0 \end{bmatrix} r.
\end{aligned} \tag{13}
$$

This equation is then solved iteratively using Equations 4 to 6.

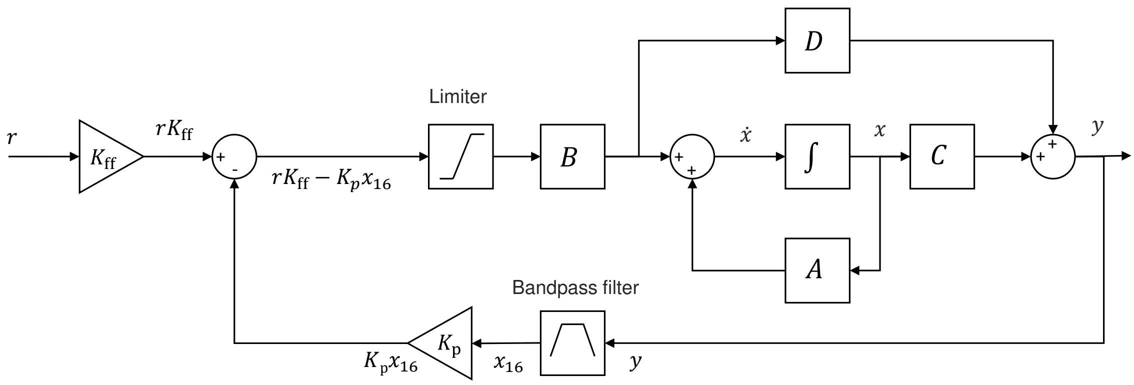

Figure 3: Schematic of the closed-loop system in state-space representation. The command signal r is scaled by the feedforward gain K_{ff}. In parallel, the measured sensor voltage $x_2 = u_{C_{\mathrm{ps}}}$ is passed through a second-order bandpass filter state x_{16} and scaled by the feedback gain K_p. The combined control input $u_{C_{\mathrm{pa}}} = K_{\mathrm{ff}} r - K_p x_{16}$ drives the system.

4. Results

The transfer function from the input voltage u_{in} to the output pressure p_{out} is first calculated in the frequency domain to evaluate the influence of the feedback gain K_p and the feedforward gain K_{ff} on the pressure response at the coupler microphone. As shown in Figure 4, with $K_p = 220$ and $K_{ff} = 1.21$, the frequency response is nearly identical for both the open-loop and closed-loop cases. The only noticeable differences are a slightly increased quality factor at the loudspeaker resonance and a minor pressure gain, primarily outside the bandpass filter passband (below 20 Hz and above 1500 Hz).

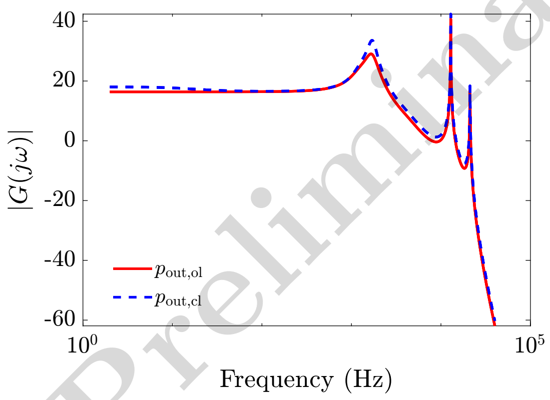

Figure 4: Open-loop and closed-loop linear frequency response of the loudspeaker coupled to the IEC 60318-4 ear simulator.

The total harmonic distortion (THD) generated by the loudspeaker is evaluated by sweeping pure sine signals across the audible frequency range. Figure 5 compares the THD in the occluded-ear coupler for both the open-loop and closed-loop configurations, using an AC actuation voltage of 7 V and a DC bias of 15 V. The results demonstrate that the closed

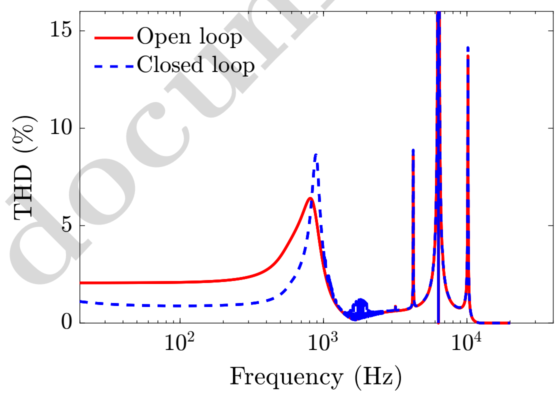

Figure 5: Total harmonic distortion of the loudspeaker in open loop and closed loop configurations.

loop reduces the THD by half at lower frequencies. The slight increase in THD around the loudspeaker's resonance frequency is attributed to the change in the quality factor induced by the feedback loop.
For a physical implementation, system noise must be taken into account, and the high permittivity of the PZT material could potentially limit sensor performance. Additionally, because the phase shift above the driver's resonance frequency mandates the use of a bandpass filter, the THD is not reduced at higher frequencies, however, it remains undegraded.

5. Conclusions

This work presented a modeling framework for a MEMS loudspeaker equipped with a collocated piezoelectric sensor and actuator, operated under active feedback control. An analytical beam model was developed and validated against finite-element simulations to derive the transduction factors and apparent compliance of the device, which were then embedded into a multi-domain lumped-element state space model coupled to an IEC 60318-4 ear simulator. The comparison between the open-loop and closed-loop responses indicates that the feedback scheme reduces the total harmonic distortion while preserving the acoustic performance of the device, supporting the feasibility of active control for compact MEMS transducers intended for in-ear applications.

Acknowledgments

The authors would like to thank their colleagues at CEA-Leti for their support during the development of this work.

References

[1] N. Wittek, A. Melnikov, B. Kaiser, and A. Zimmermann, "Review of mems speakers for audio applications," *arXiv preprint arXiv:2512.17708*, 2025.

[2] L. Fielder and E. Benjamin, "Subwoofer Performance for Accurate Reproduction of Music," English, *JAES Volume 36 Issue 6*, Jun. 1988.

[3] B. Dukes, "Audio Engineering Society," en, p. 4, 2012.

[4] S. Temme, P. Brunet, and P. Qarabaqi, "Measurement of Harmonic Distortion Audibility Using a Simplified Psychoacoustic Model - Updated," en, p. 9, 2013.

[5] S. Weng, S. Pawar, and J. H. Huang, "Magnetic motor nonlinearity modifications for total harmonic distortion improvement of an elliptical miniature loudspeaker," *IEEE transactions on magnetics*, vol. 48, no. 12, pp. 4811–4814, 2012.

[6] Q. Zheng et al., "Spl and thd improvement of a cantilever-diaphragm piezoelectric mems loudspeaker with double-s actuators," *Microsystems & Nanoengineering*, vol. 11, no. 1, p. 167, 2025.

[7] D. Tumpold, M. Stark, N. Euler-Rolle, M. Kaltenbacher, and S. Jakubek, "Linearizing an electrostatically driven mems speaker by applying pre-distortion," *Sensors and Actuators A: Physical*, vol. 236, pp. 289–298, 2015.

[8] H. Schurer, A. P. Berkhoff, C. H. Slump, and O. E. Herrmann, "Modeling and compensation of nonlinear distortion in horn loudspeakers," in *Proceedings of the 96th convention of the Audio Engineering Society*, 1994.

[9] O. Massi, A. I. Mezza, R. Giampiccolo, and A. Bernardini, "Learning piezoelectric hysteresis in in-ear mems loudspeakers from acoustic measurements," in *ICASSP 2026-2026 IEEE International Conference on Acoustics, Speech and Signal Processing (ICASSP)*, IEEE, 2026, pp. 15 992–15 996.

[10] Y. Kadowaki and T. Samejima, "Nonlinear distortion reduction of an electrodynamic loudspeaker by using model-following control theory," *Acoustical Science and Technology*, vol. 38, no. 4, pp. 222–224, 2017.

[11] P. Frigerio et al., "Nested closed-loop control of quasi-static mems scanners with large dynamic range," *IEEE Transactions on Industrial Electronics*, vol. 70, no. 4, pp. 4217–4225, 2022.

[12] R. Liechti, S. Durand, T. Hilt, F. Casset, C. Dieppedale, and M. Colin, "High performance piezoelectric mems loudspeaker based on an innovative wafer bonding process," *Sensors and Actuators A: Physical*, vol. 358, p. 114 413, 2023.

[13] R. Liechti, "Development of a mems loudspeaker with optimized performance," Ph.D. dissertation, Le Mans Université, 2022.

[14] R. Liechti, "Equivalent electrical circuits for electroacoustic mems design: A review," *Journal of Micromechanics and Microengineering*, vol. 34, no. 8, p. 083 004, 2024.

[15] R. Liechti et al., "A piezoelectric mems loudspeaker lumped and fem models," in *2021 22nd International Conference on Thermal, Mechanical and Multi-Physics Simulation and Experiments in Microelectronics and Microsystems (EuroSimE)*, IEEE, 2021, pp. 1–8.

[16] R. Liechti et al., "Total harmonic distortion of a piezoelectric mems loudspeaker in an iec 60318-4 coupler estimation using static measurements and a nonlinear state space model," *Micromachines*, vol. 12, no. 12, p. 1437, 2021.